Atmos. Chem. Phys. Discuss., 9, 20853–20880, 2009
www.atmos-chem-phys-discuss.net/9/20853/2009/

Atmospheric Chemistry and Physics Discussions

This discussion paper is/has been under review for the journal *Atmospheric Chemistry and Physics (ACP)*. Please refer to the corresponding final paper in *ACP* if available.

Effects of absorbing aerosols in cloudy skies: a satellite study over the Atlantic Ocean

K. Peters[1,2], **J. Quaas**[1], **and N. Bellouin**[3]

[1]Max Planck Institute for Meteorology, Hamburg, Germany
[2]University of Hamburg, Hamburg, Germany
[3]Hadley Centre, Met Office, Exeter, UK

Received: 25 August 2009 – Accepted: 13 September 2009 – Published: 2 October 2009

Correspondence to: K. Peters (karsten.peters@zmaw.de)

Published by Copernicus Publications on behalf of the European Geosciences Union.

Abstract

Aerosol effects, direct as well as indirect, constitute one of the biggest sources of uncertainty when it comes to quantifying human forcing of climate change. Understanding these will thus increase the credibility of climate predictions. This study focuses on aerosol effects when absorbing aerosols reside in cloudy skies. In cloudfree conditions, aerosols usually exert a negative radiative forcing (RF) at the top of the atmosphere (TOA) due to their scattering properties. When located above clouds, absorbing aerosols can reduce the shortwave local planetary albedo α, resulting in an often significant local positive direct radiative forcing (DRF). A method for deriving the aerosol radiative effects of absorbing aerosols in cloudy situations from satellite retrievals is presented. Data of 2005 and 2006 from various sensors aboard satellites of the "A-Train" constellation, restricted to the tropical and subtropical Atlantic ocean, is used. A multiple linear regression is performed to identify the dependence of α in cloudy scenes on cloud liquid water path (LWP) and aerosol optical depth (AOD), using the OMI UV-Aerosolindex (UV-AI) as an indicator for absorbing aerosols. The results show an increase of α with increasing aerosol load, and a relative decrease of α with increasing amount of absorbing aerosols in cloudy scenes. This allows to derive the direct aerosol effect of absorbing aerosols above clouds, with the effect of aerosol absorption over clouds in the Atlantic contributing $+0.08 \pm 1.2 \times 10^{-3}$ Wm^{-2} to the global TOA RF.

1 Introduction

Aerosols are an important constituent of the climate system due to their effect on the radiation budget of the atmosphere. Aerosols can interact with radiation directly, by absorption and scattering (Ångström, 1962; McCormick and Ludwig, 1967), or indirectly through the modification of cloud microphysical properties (Twomey, 1974; Devasthale et al., 2005, 2006), possibly leading to the so-called cloud-lifetime effect (Albrecht,

ACPD

9, 20853–20880, 2009

1989; Pincus and Baker, 1994). Absorbing aerosols have been found to exert a so-called semi-direct effect, altering the average cloud fraction by locally heating cloud- and near-cloud air layers (Hansen et al., 1997; Johnson et al., 2004). Understanding the underlying mechanisms of the climate system and its change under anthropogenic influence is a big challenge. Assessing the role of aerosols in this system has been a major effort by measurement campaigns as well as remote sensing and modelling studies. Nevertheless, the exact mechanisms and effects of aerosols on climate are still not well understood. This results in large uncertainties when quantifying anthropogenic radiative forcing of climate change (IPCC, 2007). The aim of this study is to investigate the radiative forcing at the top of the atmosphere (TOA) of absorbing aerosols in cloudy situations. Analysis will be performed by means of satellite retrievals for the Atlantic ocean region. The single scattering albedo (SSA) ω_0 is the ratio of scattering to total extinction. Even for highly absorbing aerosol (with ω_0 as low as 0.8), scattering dominates extinction in the visible spectral range. In clear sky conditions, even strongly absorbing aerosols usually impose a negative TOA DRF over oceanic regions due to the dark underlying surface. An observer from space would see this as an apparent "brightening" of the overall scene. Increase of the underlying surface albedo, such as clouds residing below aerosols, alters the appearance of this scene from space quite remarkably: for absorbing aerosol, a reduction of brightness, a darkening, of the overall scene would be observed from space, implying a positive TOA DRF. In this case, the absorption of the particle dominates the scattering for the net TOA effect. Therefore, the net TOA radiative effect of a specific absorbing aerosol depends on the underlying surface albedo. Previous measurement and modeling studies of these situations confirm this deduction, mainly using a cloud layer underlying aerosols as a proxy for high surface albedo. Liao and Seinfeld (1998a,b) have shown, by use of a one-dimensional column model, that the DRF of dust aerosol becomes positive in the presence of a cloud layer. This effect becomes largest with the aerosol layer overlying a cloud layer of large cloud optical thickness. Haywood and Shine (1997) used a multi-spectral radiation code to calculate similar situations for soot, yielding similar results for soot over-

lying a cloud layer. Emphasis is put on the vertical distribution of clouds and aerosols in GCM calculations to correctly infer anthropogenic DRF. Keil and Haywood (2003) used field measurements of the SAFARI-2000 campaign to calculate DRF of biomass burning aerosol residing above closed stratocumulus decks off the coast of Namibia and Angola. Assuming no effect of the aerosol on the clouds themselves, the presence of clouds converted the original negative TOA DRF to a positive one of nearly the same magnitude (from -13.0 Wm^{-2} to $+11.5$ Wm^{-2}). Using satellite retrievals only, Stammes et al. (2008) investigated the same region with respect to absorbing aerosol presence in cloudy scenes. A shortwave heating of the atmosphere in the range of 0 to $+80$ Wm^{-2}, with a mean of $+35$ Wm^{-2}, is found by comparing reflectance spectra of clean and polluted scenes. Most recently, Chand et al. (2009) studied the same region by combining data measured from different satellite sensors and radiative transfer calculations to infer a more thorough picture of the radiative forcing (RF) patterns for the period of July–October 2006 and 2007. They found that the sign of DRF exerted by absorbing aerosols above clouds depends on cloud fraction, with the forcing being positive and up to $+12$ Wm^{-2} on regional scales. The critical cloud fraction is proposed to be about 0.4, with positive forcing occurring for larger values. Satellite data nowadays offer the opportunity to investigate global distributions of aerosols and clouds on long temporal timescales. Measurements of instruments on satellites in the "A-Train" constellation (Stephens et al., 2002; Anderson et al., 2005) yield excellent coincidence in time and space. In this study, data from four different instruments of the A-Train constellation are combined. The data used in this study is presented in Sect. 2. The method and results of deriving a quantitative relationship of cloudy scene α and AOD are presented and discussed in Sect. 3. Method and results of the radiative forcing calculations are shown and discussed in Sect. 4. Finally, the results are summarised and conclusions are drawn in Sect. 5.

2 Data

The A-Train satellite constellation currently consists of five satellites which orbit the Earth in formation (Stephens et al., 2002; Anderson et al., 2005), where the time difference between the first satellite, EOS (Earth Observing System) Aqua, and the last satellite, EOS Aura, is eight minutes. One main advantage of the A-Train is the possibility of combining all measured data due to the collocation in time and space. The aim of this study is to combine measurements of cloud, aerosol and radiative properties to then derive the TOA RF of absorbing aerosols in cloudy scenes. Data covering the Atlantic Ocean from 35° N to 30° S at a resolution of 0.25°×0.25° for the years 2005 and 2006 are used. The data products of the A-Train constellation used in this study are introduced in the following.

2.1 MODIS

MODIS (MODerate resolution Imaging Spectrometer) on EOS Aqua measures the upwelling radiance in 36 channels within the spectral range from 0.44 to 15 μm. Due to its wide swath, it is possible to achieve global coverage almost every day. Seven of the MODIS channels, in the spectral range from 0.47 to 2.13 μm, can be used to obtain aerosol optical properties in cloud free ocean as well as over suited land scenes (King et al., 1992; Kaufman et al., 1997; Tanré et al., 1997; Yu et al., 2006). Measurements of the AOD over cloud-free oceans allow for a precision of ±0.03 ±0.05 τ, mainly due to assumptions made in the radiative transfer model applied. The retrieval algorithm additionally provides the AOD fine-mode fraction which is that part of the extinction which can be associated to small particles. The MODIS data products used in this study are the MYD08_D3 and MYDATML2 collection 5 datasets as obtained from the MODIS website (NASA MODIS). AOD in this study is from the MYD08_D3 daily Level3 product on a 1°×1°grid. For the further analysis, the data is interpolated to 0.25°×0.25°. The MYDATML2 product provides the retrievals of cloud fraction and cloud-top temperature used in this study at high resolution, which we average to a 0.25°×0.25°global grid.

ACPD
9, 20853–20880, 2009

In this study, aerosol properties from the coarse resolution product (MYD08_D3) are combined with cloud parameters from the finer resolution product, assuming that the aerosol is homogeneously distributed in a 1°×1°grid box. Variations in aerosol properties, in contrast to cloud properties, tend to occur on spatial scales spanning a few hundred kilometres, especially over oceans (Anderson et al., 2003). Therefore, reduction of resolution of the aerosol compared to the cloud data will not introduce significant uncertainties in the analysis.

2.2 AMSR-E

AMSR-E (Advanced Microwave Scanning Radiometer – Earth Observing System; Kawanishi et al., 2003) is installed on EOS Aqua and provides global passive microwave measurements. Horizontally and vertically polarised brightness temperatures are measured in six channels, from 6.9 GHz to 89.0 GHz and the spatial resolution varies from 5.4 km at 89 GHz to 56 km at 6.9 GHz. Important for this study is the derivation of the cloud liquid water path (LWP) from AMSR-E measurements at 36.5 GHz (Wentz, 1997). The data used is gridded onto a global 0.25°×0.25°grid and obtained from the website www.remss.com.

2.3 CERES

CERES (Clouds and the Earth's Radiant Energy System; Wielicki et al., 1996; Loeb and Manalo-Smith, 2005) is an instrument aboard EOS Aqua and is designed to measure the upwelling short- and longwave radiation at about 20×20 km^2 horizontal resolution. The measured radiances are converted into TOA fluxes as a function of viewing- and solar zenith angles by the use of Angular Distribution Models (ADMs) and allow for a detailed computation of the Earth's radiation budget. The CERES dataset used in this study is the single-scanner-footprint (SSF) product CER_SSF_Aqua-FM3-MODIS_Edition2A. This Level2 dataset is a combination of MODIS and CERES measurements. The only parameter used in this study is the spectrally averaged (0.3–

5 μm), upwelling shortwave radiative flux at TOA (CERES_SW_TOA_flux_-_upwards), which we convert into local planetary albedo α by relating the outgoing shortwave flux to the expected instantaneous incoming solar insolation computed by use of the CERES measured solar zenith angle at the surface, the eccentricity of Earth's orbit and a solar constant of 1365 Wm^{-2}. The data is, like the MODIS Level2 data, gridded onto a 0.25°×0.25°global grid.

2.4 OMI

OMI (Ozone Monitoring Instrument) is a spectrally highly resolving spectrometer installed on EOS Aura which is capable of measuring radiation in the UV and visible spectral range (0.27–0.5 μm) reflected by the Earth System. It is the follow-up of TOMS (Total Ozone Mapping Spectrometer; Heath et al., 1975), has a swath width of 2600 km and offers nearly daily global coverage with a spatial resolution ranging from 13×24 km^2 to 28×150 km^2. The main advantage of OMI for this study is, that aerosol properties can be derived from its measurements in the UV spectral range also in cloudy scenes. Retrieval algorithms originally developed for TOMS are used to derive the so-called UV-Aerosol Index (UV-AI) (Torres et al., 1998; de Graaf et al., 2005). The properties of this index are important in the context of this study and will be explained later in the text. The UV-AI is taken from the OMAERUVG_v003 dataset, which is a gridded dataset supplying all measurements falling into a 0.25°×0.25°gridbox (Leonard, 2008). For further processing, the simple mean of all measurements in one grid box is calculated.

2.4.1 The UV-AI

The UV-AI is a semi-quantative measure allowing for sampling of radiative properties of aerosols in the UV. It is derived by relating the measured upwelling radiances at two wavelengths in the UV (342.5 and 388 nm for OMI; Levelt et al., 2002) to those calculated by a radiative transfer model assuming molecular scattering only (Torres

et al., 1998; de Graaf et al., 2005). Radiative transfer calculations show that the UV-AI takes positive values for absorbing aerosol, negative values for non-absorbing aerosol and zero for clouds or purely molecular scattering (Torres et al., 1998; de Graaf et al., 2005). An advantage of the UV-AI is that it allows to detect the absorption due to the presence of the aerosol layer independently from the brightness of the overall scene in the visible spectral range. Thus it is possible to detect absorbing aerosols over and in clouds as well as over snow- or ice-covered land surfaces (Levelt et al., 2002; Torres et al., 2007). It is interesting to investigate whether a proportionality between the UV-AI and AOD over ocean areas exists. AOD and UV-AI correlate very well when investigating situations with just one prevailing aerosol type and near homogeneous surface brightness (desert dust, biomass burning smoke; Hsu et al., 1999), as the UV-AI explicitly depends on aerosol species, the height above the underlying surface (or cloud) as well as on the overall brightness of the observed scene (Torres et al., 1998; de Graaf et al., 2005). The same is found by Christopher et al. (2008) who additionally find the correlation between AOD and UV-AI getting significantly weaker over oceanic areas due to mixing of aerosol types. Results of this study shown in Fig. 1 support these findings. According to theory, the UV-AI should be close to unity for very low AOD values. Histograms for the regions of interest (see Fig. 2 and Table 1 for region definitions) are displayed in Fig. 1, where the number of measurements in each UV-AI bin (ΔUV-AI=0.015) is plotted. The PDs in Fig. 1 show a peak at $0 \leq$UV-AI<0.015, but also a large number of measurements falling into the range of $0.1 \leq$UV-AI<0.7. Thus, in accordance with Torres et al. (1998); de Graaf et al. (2005) and Christopher et al. (2008), it is not possible to infer a quantitative relationship between measured AOD and UV-AI values when the aerosol species observed cannot be characterised. Here, uncertainties for low aerosol burdens with the former possibly stemming from mixing of aerosol species may certainly play a role.

Sensitivity of the UV-AI to key parameters

As mentioned above, the UV-AI is dependent on a number of boundary conditions. de Graaf et al. (2005) show calculations of the sensitivity of the UV-AI to parameters such as the solar zenith angle or the surface albedo. Using aerosol layer parameters representative for naturally occurring conditions, the UV-AI shows a strong dependence on the surface albedo for high solar zenith angles. The UV-AI can thus only be considered as independent of the surface albedo for solar zenith angles θ_0<45°. Furthermore, the dependence of the UV-AI on the AOD of the aerosol layer is tested and found to be nearly linear and identical for all calculations with $\theta_0 \leq 60°$. To account for these dependencies, the results of de Graaf et al. (2005) therefore lead to the choice of using measurements (of all instruments) with solar zenith angles $\theta_0 \leq 45°$ in the present study, only. Additionally, a restriction concerning the viewing geometry of the OMI instrument is taken into account. Calculations of de Graaf et al. (2005) show, that the value of the UV-AI is dependent on the viewing zenith angle. It is stated, that values of the UV-AI quickly increase with viewing zenith angles >60°. In combination with the above mentioned threshold for the solar zenith angle, the threshold for the viewing zenith angle is chosen in such a way, that only scenes with a viewing zenith angle of <30°are allowed for further analysis. The restrictions applied reduce the amount of measurements available for the regression by roughly 15% and it is assured that derived UV-AI values for a large scale aerosol layer of homogeneous properties do not vary significantly within the area observed.

3 Statistical analysis of overcast scenes

3.1 Method

The aim of this study is to analyse the effects of absorbing aerosols in cloudy skies using satellite retrievals. A two year time frame spanning dataset over the tropical

ACPD
9, 20853–20880, 2009

and subtropical Atlantic Ocean is used to derive statistical relationships between the aerosol concentration and changes of the local planetary albedo α of a scene. Focus is put to the Atlantic ocean, as this region is often influenced by absorbing aerosol pollution (e.g. Saharan dust and biomass burning). Only oceanic regions are used, since measurements of the LWP from AMSR-E are not available over land. We choose here not to use the CALIOP (Cloud-Aerosol Lidar with Orthogonal Polarization; Kim et al., 2008), since it covers only a very narrow swath, and since examination of the available data products show ambiguous results on cloud and aerosol layers. Nevertheless, Chand et al. (2009) have used CALIOP measurements to investigate vertically separated aerosol and cloud layers, assuming aerosol properties being homogeneous in a 5°×5°domain. In this study, data from MODIS and OMI is used to check for absorbing aerosols in cloudy situations. Cloud properties are taken from the fine resolution MODIS product, AOD from the coarse resolution aggregated MODIS product and the UV-AI from the above mentioned OMI product. It is assumed that AOD retrieved by MODIS in clear parts of a 1°×1°grid box of the coarse resolution MODIS product are representative for the entire grid-box and not being subject to significant subgrid scale variability (Anderson et al., 2003). Since we are interested in liquid water clouds, we select scenes overcast with clouds with a cloud top temperature greater than 273.15 K. Then, the AOD and the UV-AI for this scene are used to characterise the aerosol.

Accounting for differences in the aerosol characteristics with respect to geographical location is achieved by dividing the tropical and subtropical Atlantic Ocean into different areas. Aerosol characteristics in each area are assumed to be similar on seasonal timescales. The classification of areas is displayed in Fig. 2 with the acronyms explained in Table 1.

The relationship between observed α and absorbing aerosol mass is computed by means of a multiple linear regression. α of a scene overcast with a liquid water cloud depends on the surface albedo, cloud liquid water path, and AOD, with the latter also influencing cloud droplet number concentration through the first aerosol indirect or Twomey effect (Twomey, 1974). We represent α in scenes overcast with liquid water

clouds in terms of the natural logarithm of LWP and AOD by a multiple linear regression of the form

$$\alpha = a_0 + a_1 \ln(\mathrm{LWP}) + a_2 \ln(\mathrm{AOD}) \quad (1)$$

with α being derived from CERES TOA shortwave flux, LWP the cloud liquid water path from AMSR-E and AOD the aerosol optical depth from the coarse resolution MODIS dataset. All three quantities are derived from independent coincident retrievals. The LWP retrievals in the microwave spectral range are less affected by aerosol radiation interactions than retrievals in the visible spectrum, thus yielding better results for cloud properties in aerosol contaminated scenes (Wilcox et al., 2009; Chellappan and Horváth, 2009). The UV-AI is used for a conditional sampling of the scenes. We choose a threshold value of UV-AI=0.7 to distinguish between absorbing (UV-AI >0.7) and non-absorbing (UV-AI <0.7) aerosols (M. de Graaf, KNMI, personal communication, 2008). The multiple-regression coefficients a_0, a_1 and a_2 are then calculated for the two UV-AI bins for all four regions as follows: In order to get an error estimate, regressions are performed for slabs of 1000 randomly picked measurement triplets (α, LWP and AOD) of each region. We define the regression slope error as the standard deviations of the 10–100 slopes offered by this approach for each of the four regions. Applying this method, possible dependencies on large scale meteorological conditions (e.g. seasonal change in tropical circulation patterns) and intra-regional variations in background conditions are taken into account.

3.2 Results

We are interested here in detecting a relationship between the absorbing aerosol concentrations and changes of α cloudy situations. The regions investigated in this study are frequently influenced by absorbing aerosols. These aerosols are mainly injected into the atmosphere over land (e.g. desert dust, biomass burning or industrial aerosol) and then advected over oceanic regions. The tropical Atlantic oceanic air masses are heavily influenced especially by emissions from the African continent. Therefore, the

area covered by the semipermanent stratocumulus decks off the coast of Namibia and Angola (region TSEA) can be considered as offering ideal conditions for observing absorbing aerosols above clouds, especially during the biomass burning season (Keil and Haywood, 2003; Haywood et al., 2004; Stammes et al., 2008; Chand et al., 2009). Similarly, desert dust stemming from the Sahara is very often advected over the Atlantic, leading to high absorbing aerosols loading in the region TNEA. The relative amount of measurements going into the regression analysis displayed in Table 2 shows the frequent occurrence of absorbing aerosols in cloudy scenes in the region of interest. Indeed, the two regions bordering the western coast of Africa, TSEA and TSWA, both show a higher fraction of absorbing aerosol observations than the neighbouring regions to the west. Region TNEA even shows the majority of all measurements having an UV-AI $\geq$0.7, most certainly stemming to a large extent from desert dust advected over the ocean.

The calculated values for the coefficients a_2, along with their respective standard deviations, are shown in Fig. 3. For an UV-AI <0.7, α is found to increase with AOD in all regions except for the region TSEA, where a decrease of α with AOD is derived. A positive correlation between α and AOD for scattering aerosols in cloudy scenes may be attributed to a combination of the aerosol direct effect and the increase in cloud albedo by the aerosol indirect effect. Since we stratify by LWP in the multiple regression, only the Twomey effect (first indirect effect) is considered here. Since the region TSEA is often subject to significant absorbing aerosol pollution (Stammes et al., 2008), the derived reduction of α for scenes with UV-AI <0.7 hints at frequent occurence of weakly absorbing aerosol dominating over scattering aerosol in this region. Additionally, the semipermanent stratocumulus decks topping the marine boundary layer in this region yield very low cloud top heights, making it difficult for the advected aerosol to get entrained (Keil and Haywood, 2003). By this, the indirect aerosol effect, which would lead to a positive coefficient a_2 like in the other regions, is inhibited.

For scenes with an UV-AI >0.7, negative coefficients a_2 are calculated for all regions considered. This is expected, since an increasing absorbing aerosol concentration in

cloudy scenes leads to a reduction of α at TOA especially for aerosols above clouds. Here, the reduction of α with AOD is strongest for the region TNWA, with region TSEA showing just litte less reduction. Region TNEA is subject to the least reduction of α in the spectral range measured by CERES. This region is suspected to be heavily influenced by Saharan dust aerosols, which have a significantly higher absorption in the UVA spectral range than in the visible (Bergstrom et al., 2007). A large UV-AI for dust may correspond to only a weak absorption in the visible range, for which α is defined.

4 Radiative forcing calculations

4.1 Method

The TOA radiative forcing by anthropogenic absorbing aerosols, F_{ant}, can be computed as

$$F_{ant} = \bar{F}\ \Delta\alpha_{ant}\ \mathrm{LCF}, \tag{2}$$

with $\bar{F}$ being the incoming daily mean TOA solar radiation, LCF the liquid cloud fraction and $\Delta\alpha_{ant}$ the change in local planetary albedo defined as

$$\Delta\alpha_{ant} = \alpha_{tot} - \alpha_{nat}, \tag{3}$$

with

$$\alpha_{nat} = a_0 + a_1 \ln(\mathrm{LWP}) + a_2 \ln(\mathrm{AOD}_{tot} - \mathrm{AOD}_{ant}), \tag{4}$$

and

$$\alpha_{tot} = a_0 + a_1 \ln(\mathrm{LWP}) + a_2 \ln(\mathrm{AOD}_{tot}), \tag{5}$$

where AOD_{tot} is the total AOD and AOD_{ant} the anthropogenic AOD derived by Bellouin et al. (2005), updated with MODIS collection 5 data. All the data which was previously

ACPD
9, 20853–20880, 2009

used to derive the coefficients a_0, a_1 and a_2 in Eq. (1) is used for the forcing calculations. Firstly, the radiative forcing by all anthropogenic aerosols in scenes overcast with liquid water clouds is computed choosing the regression applicable according to the retrieved UV-AI. Secondly, the absorption effect by anthropogenic aerosols is separated using a coefficient $a_{2_{\text{eff}}}$ defined as

$$a_{2_{\text{eff}}} = a_2|_{\geq 0.7} - a_2|_{<0.7}, \quad (6)$$

with $a_2|_{<0.7}$ and $a_2|_{\geq 0.7}$ being the calculated coefficients for scenes with an UV-AI < 0.7 and ≥ 0.7, respectively. Only situations influenced by absorbing aerosol, defined by an UV-AI ≥ 0.7, are used for the second setup, with the absorption forcing considered zero in all other scenes.

This RF is calculated for each of the regions and seasons described in Table 1. A distinction between seasons is made to distinguish prevailing aerosol types such as the biomass burning season in southern Africa.

4.2 Results

Table 3 presents the resulting yearly averaged total and absorbing RF by anthropogenic aerosols weighted by the area coverage of each region, defined as the fraction of the globe covered by this region.

The regions TNWA, TNEA and TSWA, show negative TOA RF. This suggests that aerosol scattering and the aerosol indirect effect dominate aerosol absorption. The calculated TOA RF for the region TSEA is positive and much larger than the negative forcing of the other regions. Comparing the RF values of the separate regions, the forcing of the subtropical and tropical Atlantic is dominated by region TSEA, suggesting the radiative properties of this region being important even on a global scale. The same holds when considering the results for the effect of just the aerosol absorption. As previous studies of the radiative effects of absorbing aerosols above clouds have mostly focused on the region off the southern coast of Africa, the results of region TSEA are displayed in more detail in Table 4.

It is evident, that the TOA RF of absorbing aerosols in cloudy scenes in region TSEA is subject to a pronounced seasonal cycle, with a distinct maximum occurring during the time of June–November. On a global scale, the TOA RF can reach up to $+0.14\pm0.02$ Wm^{-2}. This is, even on a global scale, not negligible regarding the estimates of the direct aerosol effect presented in IPCC (2007), which range from -0.9 Wm^{-2} to -0.1 Wm^{-2}, with a best estimate of -0.5 Wm^{-2}. Locally, the radiative forcing can exceed $+40$ Wm^{-2}, with a mean regional TOA anthropogenic RF of $+4.34\pm0.58$ Wm^{-2} and $+3.04\pm0.64$ Wm^{-2} in season JJA and SON, respectively. The effect of aerosol absorption coming from heavily absorbing aerosols on the TOA RF alone is calculated to account for the largest part of the total TOA RF, especially during the biomass burning season. During months JJA, the effect of aerosol absorption accounts for roughly 75% of the total TOA RF. The months June–November correspond to the biomass burning season in southern Africa, giving rise to large scale elevated aerosol layers above the semipermanent stratocumulus decks off the coast (Keil and Haywood, 2003). Therefore, the change of magnitude in DRF is subject to a pronounced seasonal cycle. The results found here are consistent with previous studies for the TSEA region (Stammes et al., 2008; Chand et al., 2009; Schulz et al., 2006; Keil and Haywood, 2003; Haywood and Shine, 1997). It should be emphasized that the forcing values presented here are the contribution of the direct and first indirect aerosol effects in cloudy skies. The direct effect in clear skies as well as semi-direct and second indirect effects would need to be taken into account for an estimate of the overall anthropogenic aerosol forcing in the region of interest.

5 Summary and conclusions

This study is aimed at investigating the direct radiative forcing (DRF) of absorbing aerosols in cloudy skies based on spaceborne measurements. A dataset covering the tropical and subtropical Atlantic Ocean, consisting of two years (2005 and 2006) of data from different satellite sensors in the "A-Train" constellation (Stephens et al.,

2002; Anderson et al., 2005), is used to perform a statistical analysis in order to find a relationship between local planetary albedo α and absorbing aerosol presence in cloudy scenes. A multiple linear regression is performed to derive a statistical expression linking α derived from CERES to cloud liquid water path (LWP) from AMSR-E and aerosol optical depth (AOD) from MODIS in presence of low-level liquid water clouds as detected by MODIS. We use the UV-Aerosol Index (UV-AI) derived from OMI data as an indicator for absorbing aerosol presence in cloudy scenes. For situations with scattering and only slightly absorbing aerosols (UV-AI <0.7), α increases with AOD in three out of four regions, which is consistent with aerosol scattering and/or an aerosol indirect effect. In scenes with absorbing aerosols (UV-AI >0.7), in all regions, α decreases with AOD, hinting at the effect of aerosol absorption in the cloudy scenes. The relationships are used to infer the RF at the top of the atmosphere (TOA) due to anthropogenic aerosols. The anthropogenic aerosol fraction is taken from the dataset described in Bellouin et al. (2005). The overall forcing is negative in three out of four regions, but positive in the TSEA region. Due to the frequent presence of low-level clouds and the strong α-AOD relationship, this region dominates the anthropogenic forcing in scenes with low-level clouds in the entire region investigated here, which amounts to a contribution to the global annual mean anthropogenic aerosol forcing by $+0.05\pm0.03\,\mathrm{Wm}^{-2}$. Within the TSEA region anthropogenic aerosols exert regional seasonal mean forcings of up to $4\,\mathrm{Wm}^{-2}$ in JJA. Concluding, absorbing aerosols exert a strong influence on planetary albedo. The contribution of absorption in cloudy scenes by anthropogenic aerosols in the tropical and subtropical Atlantic ocean region to the global anthropogenic aerosol forcing is estimated at $+0.08\pm1.2\times10^{-3}$.

Acknowledgements. AMSR-E data are produced by Remote Sensing Systems and sponsored by the NASA Earth Science REASoN DISCOVER Project and the AMSR-E Science Team. Data are available at www.remss.com. Thanks a lot to all the colleagues giving helpful advice throughout the conduction of this study, with special thanks going out to M. de Graaf, H. Grassl, Á. Horváth and S. Kinne.

The service charges for this open access publication have been covered by the Max Planck Society.

References

Albrecht, B. A.: Aerosols, Cloud Microphysics, and Fractional Cloudiness, Science, 245, 1227–1230, 1989. 20854

Anderson, T. L., Charlson, R. J., Winker, D. M., Ogren, J. A., and Holmen, K.: Mesoscale variations of tropospheric aerosols, J. Atmos. Sci., 60, 119–136, 2003. 20858, 20862

Anderson, T. L., Charlson, R. J., Bellouin, N., Boucher, O., Chin, M., Christopher, S. A., Haywood, J., Kaufman, Y. J., Kinne, S., Ogren, J. A., Remer, L. A., Takemura, T., Tanré, D., Torres, O., Trepte, C. R., Wielicki, B. A., Winker, D. M., and Yu, H. B.: An "A-Train" strategy for quantifying direct climate forcing by anthropogenic aerosols, B. Am. Meteorol. Soc., 86, 1795–1809, doi:10.1175/BAMS-86-12-1795, 2005. 20856, 20857, 20868

Ångström, A.: Atmospheric turbidity, global illumination and planetary albedo of the earth, Tellus, 14, 435–450, 1962. 20854

Bellouin, N., Boucher, O., Haywood, J., and Reddy, M. S.: Global estimate of aerosol direct radiative forcing from satellite measurements, Nature, 438, 1138–1141, 2005. 20865, 20868

Bergstrom, R. W., Pilewskie, P., Russell, P. B., Redemann, J., Bond, T. C., Quinn, P. K., and Sierau, B.: Spectral absorption properties of atmospheric aerosols, Atmos. Chem. Phys., 7, 5937–5943, 2007, http://www.atmos-chem-phys.net/7/5937/2007/. 20865

Chand, D., Wood, R., Anderson, T. L., Satheesh, S. K., and Charlson, R. J.: Satellite-derived direct radiative effect of aerosols dependent on cloud cover, Nat. Geosci., 2, 181–184, doi:10.1038/ngeo437, 2009. 20856, 20862, 20864, 20867

Chellappan, S. and Horváth, A.: Global Assessment of AMSR-E and MODIS Cloud Liquid Water Path Retrievals in Warm Oceanic Clouds, J. Geophys. Res., submitted, 2009. 20863

Christopher, S. A., Gupta, P., Haywood, J., and Greed, G.: Aerosol optical thicknesses over North Africa: 1. Development of a product for model validation using Ozone Monitoring Instrument, Multiangle Imaging Spectroradiometer, and Aerosol Robotic Network, J. Gephys. Res.-Atmos., 113, D00C04, doi:10.1029/2007JD009446, 2008. 20860

de Graaf, M., Stammes, P., Torres, O., and Koelemeijer, R.: Absorbing Aerosol Index: Sensi-

tivity analysis, application to GOME and comparison with TOMS, J. Geophys. Res.-Atmos., 110, D01201, doi:10.1029/2004JD005178, 2005. 20859, 20860, 20861
Devasthale, A., Krüger, O., and Grassl, H.: Change in Cloud-Top Temperatures Over Europe, IEEE Geosci. Remote S., 2, 333–336, doi:10.1109/LGRS.2005.851736, 2005. 20854
Devasthale, A., Kruger, O., and Grassl, H.: Impact of ship emissions on cloud properties over coastal areas, Geophys. Res. Lett., 33, L02811, doi:10.1029/2005GL024470, 2006. 20854
Hansen, J., Sato, M., and Ruedy, R.: Radiative forcing and climate response, J. Geophys. Res.-Atmos., 102, 6831–6864, 1997. 20855
Haywood, J., Osborne, S. R., and Abel, S. J.: The effect of overlying aerosol layers on remote sensing retrievals of cloud effective radius and cloud optical depth, Q. J. Roy. Meteor. Soc., 130, 779–800, 2004. 20864
Haywood, J. M. and Shine, K. P.: Multi-spectral calculations of the direct radiative forcing of tropospheric sulphate and soot aerosols using a column model, Q. J. Roy. Meteor. Soc., 123, 1907–1930, 1997. 20855, 20867
Heath, D., Krueger, A., Roeder, H., and Henderson, B.: Solar backscatter and Ultraviolet and Total Ozone Mapping Spectrometer (SBUV-TOMS) for Nimbus G, Opt. Eng., 14, 323–331, 1975. 20859
Hsu, N., Herman, J., Torres, O., Holben, B., Tanre, D., Eck, T., Smirnov, A., Chatenet, B., and Lavenu, F.: Comparisons of the TOMS aerosol index with Sun-photometer aerosol optical thickness: Results and applications, J. Gephys. Res.-Atmos., 104, 6269–6279, 1999. 20860
IPCC: Summary for Policymakers, in: Climate Change 2007: The Physical Science Basis. Contribution of Working Group I to the Fourth Assessment Report of the Intergovernmental Panel on Climate Change, edited by: Solomon, S., Qin, D., Manning, M., Chen, Z., Marquis, M., Averyt, K., M.Tignor, and Miller, H., Cambridge University Press, Cambridge, UK and New York, NY, USA, 2007. 20855, 20867
Johnson, B., Shine, K., and Forster, P.: The semi-direct aerosol effect: Impact of absorbing aerosols on marine stratocumulus, Q. J. Roy. Meteor. Soc., 130, 1407–1422, doi:10.1256/qj.03.61, 2004. 20855
Kaufman, Y. J., Tanré, D., Remer, L. A., Vermote, E. F., Chu, A., and Holben, B. N.: Operational remote sensing of tropospheric aerosol over land from EOS moderate resolution imaging spectroradiometer, J. Geophys. Res.-Atmos., 102, 17051–17067, 1997. 20857
Kawanishi, T., Sezai, T., Ito, Y., Imaoka, K., Takeshima, T., Ishido, Y., Shibata, A., Miura, M., Inahata, H., and Spencer, R.: The Advanced Microwave Scanning Radiometer for the Earth

Observing System (AMSR-E), NASDA's contribution to the EOS for global energy and water cycle studies, IEEE T. Geosci. Remote, 41, 184–194, doi:10.1109/TGRS.2002.808331, 2003. 20858

Keil, A. and Haywood, J.: Solar radiative forcing by biomass burning aerosol particles during SAFARI 2000: A case study based on measured aerosol and cloud properties, J. Geophys. Res.-Atmos., 108, 8467, doi:10.1029/2002JHD002315, 2003. 20856, 20864, 20867

Kim, S.-W., Berthier, S., Raut, J.-C., Chazette, P., Dulac, F., and Yoon, S.-C.: Validation of aerosol and cloud layer structures from the space-borne lidar CALIOP using a ground-based lidar in Seoul, Korea, Atmos. Chem. Phys., 8, 3705–3720, 2008, http://www.atmos-chem-phys.net/8/3705/2008/. 20862

King, M. D., Kaufman, Y. J., Menzel, W. P., and Tanré, D.: Remote sensing of cloud, aerosol, and water vapor properties from the Moderate Resolution Imaging Spectrometer (MODIS), IEEE T. Geosci. Remote, 30, 2–27, 1992. 20857

Leonard, P.: OMAERUVG File Specification Version 3, http://disc.sci.gsfc.nasa.gov/Aura/OMI/omaeruvg_v003.shtml, Online; accessed 27 August, 2008, 2008. 20859

Levelt, P. F., van den Oord, G. H. J., Hilsenrath, E., Leppelmeier, G. W., and Bhartia, P. K.: OMI Algorithm Theoretical Basis Document, Volume III; Clouds, Aerosols, and Surface UV Irradiance, KNMI, NASA and FMI, 2002. 20859, 20860

Liao, H. and Seinfeld, J.: Effect of clouds on direct aerosol radiative forcing of climate, J. Geophys. Res.-Atmos., 103, 3781–3788, 1998a. 20855

Liao, H. and Seinfeld, J. H.: Radiative forcing by mineral dust aerosols: sensitivity to key variables, J. Geophys. Res.-Atmos., 103, 31637–31645, 1998b. 20855

Loeb, N. G. and Manalo-Smith, N.: Top-of-atmosphere direct radiative effect of aerosols over global oceans from merged CERES and MODIS observations, J. Climate, 18, 3506–3526, 2005. 20858

McCormick, R. A. and Ludwig, J. H.: Climate Modification by Atmospheric Aerosols, Science, 156, 1358–1359, 1967. 20854

NASA MODIS: LAADS Web, http://ladsweb.nascom.nasa.gov/data/search.html, access: several times 2007 and 2008. 20857

Pincus, R. and Baker, M. B.: Effect of precipitation on the albedo susceptibility of clouds in the marine boundary layer, Nature, 372, 250–252, 1994. 20855

Schulz, M., Textor, C., Kinne, S., Balkanski, Y., Bauer, S., Berntsen, T., Berglen, T., Boucher, O., Dentener, F., Guibert, S., Isaksen, I. S. A., Iversen, T., Koch, D., Kirkevåg, A., Liu, X.,

Montanaro, V., Myhre, G., Penner, J. E., Pitari, G., Reddy, S., Seland, Ø., Stier, P., and Takemura, T.: Radiative forcing by aerosols as derived from the AeroCom present-day and pre-industrial simulations, Atmos. Chem. Phys., 6, 5225–5246, 2006, http://www.atmos-chem-phys.net/6/5225/2006/. 20867

Stammes, P., Tilstra, L. G., Braak, R., de Graaf, M., and Aben, E. A. A.: Estimate of Solar Radiative Forcing by Polluted Clouds Using OMI and SCIAMACHY Satellite Data, in: CURRENT PROBLEMS IN ATMOSPHERIC RADIATION (IRS 2008): Proceedings of the International Radiation Symposium (IRC/IAMAS), edited by: Nakajima, T. and Yamasoe, M. A., 577–580, Foz do Iguacu, Brazil, 3–8 August 2008, 2008. 20856, 20864, 20867

Stephens, G. L., Vane, D. G., Boain, R. J., Mace, G. G., Sassen, K., Wang, Z. E., Illingworth, A. J., O'Connor, E. J., Rossow, W. B., Durden, S. L., Miller, S. D., Austin, R. T., Benedetti, A., Mitrescu, C., and CloudSat Sci Team: The cloudsat mission and the a-train - A new dimension of space-based observations of clouds and precipitation, B. Am. Meteorol. Soc., 83, 1771–1790, doi:10.1175/BAMS-83-12-1771, 2002. 20856, 20857, 20867

Tanré, D., Kaufman, Y. J., Herman, M., and Mattoo, S.: Remote sensing of aerosol properties over oceans using the MODIS/EOS spectral radiances, J. Geophys. Res.-Atmos., 102, 16971–16988, 1997. 20857

Torres, O., Bhartia, P., Herman, J., Ahmad, Z., and Gleason, J.: Derivation of aerosol properties from satellite measurements of backscattered ultraviolet radiation: Theoretical basis, J. Geophys. Res.-Atmos., 103, 17099–17110, 1998. 20859, 20860

Torres, O., Tanskanen, A., Veihelmann, B., Ahn, C., Braak, R., Bhartia, P. K., Veefkind, P., and Levelt, P.: Aerosols and surface UV products from Ozone Monitoring Instrument observations: An overview, J. Geophys. Res.-Atmos., 112, D24S47, doi:10.1029/2007JD008809, 2007. 20860

Twomey, S.: Pollution and the planetary albedo, Atmos. Environ., 8, 1251–1256, 1974. 20854, 20862

Wentz, F. J.: A well-calibrated ocean algorithm for special sensor microwave/imager, J. Geophys. Res.-Oceans, 102, 8703–8718, 1997. 20858

Wielicki, B. A., Barkstrom, B. R., Harrison, E. F., Lee, R. B., Smith, G. L., and Cooper, J. E.: Clouds and the earth's radiant energy system (CERES): An earth observing system experiment, B. Am. Meteorol. Soc., 77, 853–868, 1996. 20858

Wilcox, E. M., Harshvardhan, and Platnick, S.: Estimate of the impact of absorbing aerosol over cloud on the MODIS retrievals of cloud optical thickness and effective radius us-

ing two independent retrievals of liquid water path, J. Geophys. Res., 114, D05210, doi:10.1029/2008JD010589, 2009. 20863

Yu, H., Kaufmann, Y. J., Chin, M., Feingold, G., Remer, L. A., Anderson, T. L., Balkanski, Y., Bellouin, N., Boucher, O., Christopher, S., DeCola, P., Kahn, R., Koch, D., Loeb, N., Reddy, M. S., Schulz, M., Takemura, T., and Zhou, M.: A review of measurement-based assessments of the aerosol direct radiative effect and forcing, Atmos. Chem. Phys., 6, 613–666, 2006, http://www.atmos-chem-phys.net/6/613/2006/. 20857

Table 1. Acronyms for the regions displayed in Fig. 2

TNWA	tropical northwest Atlantic
TNEA	tropical northeast Atlantic
TSWA	tropical southwest Atlantic
TSEA	tropical southeast Atlantic
DJF	December, January, February
MAM	March, April, May
JJA	June, July, August
SON	September, October, November

ACPD
9, 20853–20880, 2009

Table 2. Amount of measurements used for the regression analysis in Eq. (1).

Region	Total/10^5	Fractional amount of measurements UV-AI <0.7	UV-AI ≥0.7
TNWA	0.37	0.68	0.32
TNEA	0.99	0.43	0.57
TSWA	0.9	0.73	0.27
TSEA	1.85	0.56	0.44

ACPD
9, 20853–20880, 2009

Table 3. Annual mean global anthropogenic absorbing aerosol RF at TOA in cloudy scenes in Wm^{-2}. $<F_{ant}>_{meas}$ and $<F_{ant}>_{abseff}$ are the results obtained from the reference and the absorption effect calculation, respectively. Results are displayed for the whole subtropical and tropical Atlantic (All regions) as well as for each region separately.

Region	$<F_{ant}>_{meas}$	$<F_{ant}>_{abseff}$
All regions	$+0.05\pm0.03$	$+0.08\pm1.2\cdot10^{-3}$
TNWA	-0.01 ± 0.005	$+0.01\pm1.8\cdot10^{-4}$
TNEA	-0.005 ± 0.006	$+0.01\pm1.2\cdot10^{-3}$
TSWA	-0.006 ± 0.006	$+0.007\pm3.3\cdot10^{-4}$
TSEA	$+0.08\pm0.001$	$+0.05\pm0.002$

Table 4. Anthropogenic absorbing aerosol RF at TOA in cloudy scenes in Wm^{-2} for region TSEA (see Fig. 2). Results are displayed for different seasons (see Table 1), averaged on global and local scale. $<F_{ant}>_{meas}$ and $<F_{ant}>_{abseff}$ are the results obtained from the reference and the absorption effect calculation, respectively.

Season	$<F_{ant}>_{meas}$ global	$<F_{ant}>_{meas}$ local	$<F_{ant}>_{abseff}$ global	$<F_{ant}>_{abseff}$ local
MAM	$+0.02\pm6\cdot10^{-3}$	$+0.74\pm0.2$	$+0.02\pm6.1\cdot10^{-3}$	$+0.45\pm0.02$
JJA	$+0.14\pm0.02$	$+4.34\pm0.58$	$+0.11\pm4.5\cdot10^{-3}$	$+3.35\pm0.14$
SON	$+0.1\pm0.02$	$+3.04\pm0.64$	$+0.07\pm2.7\cdot10^{-3}$	$+2.04\pm0.09$
DJF	$+0.04\pm9\cdot10^{-3}$	$+1.19\pm0.27$	$+0.03\pm1\cdot10^{-3}$	$+0.77\pm0.03$

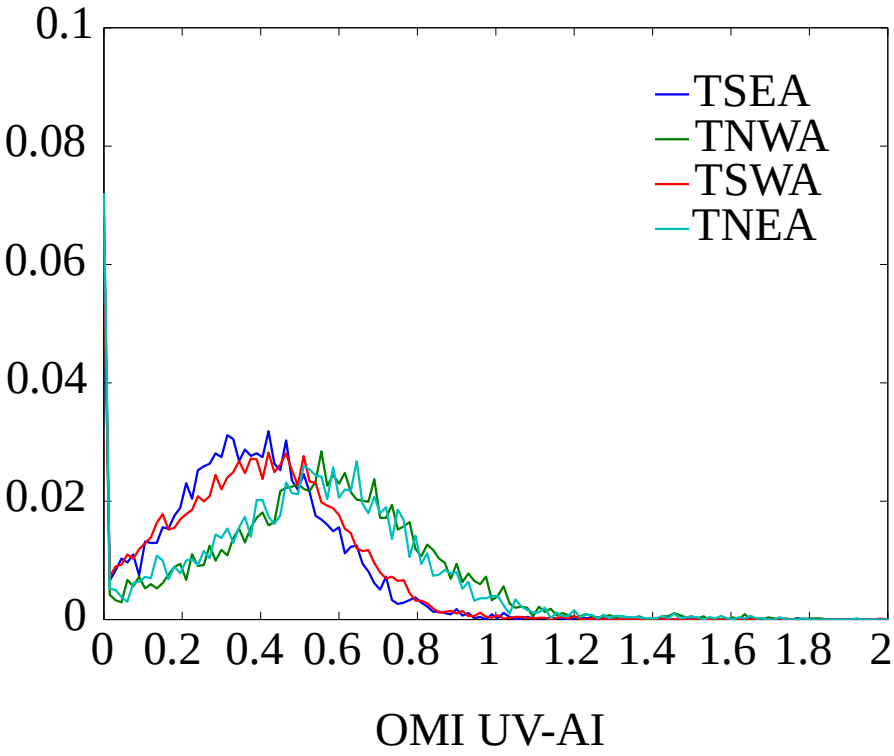

Fig. 1. Probability distribution of UV-AI measurements of the year 2005 for selected oceanic regions with Δ UV-AI=0.015 and MODIS AOD<0.05.

ACPD
9, 20853–20880, 2009

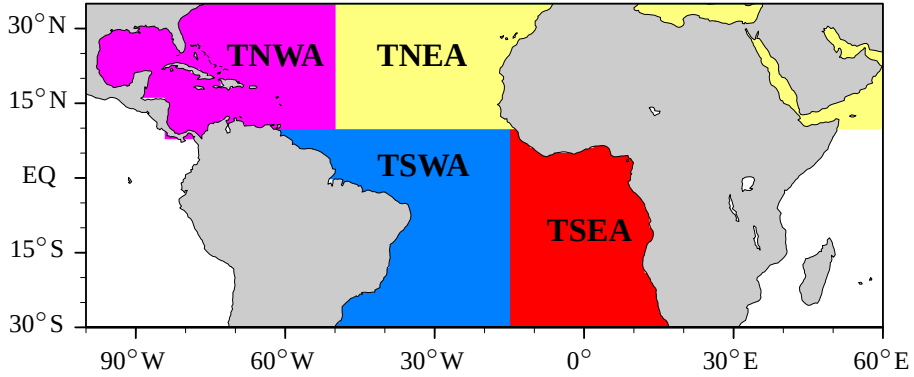

Fig. 2. Choice of different oceanic regions.

ACPD
9, 20853–20880, 2009

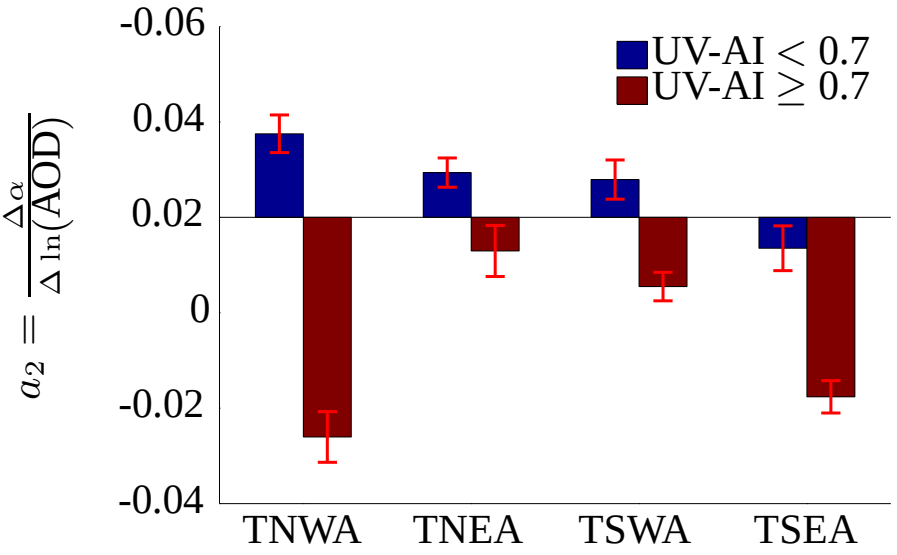

Fig. 3. Result from the regressions analysis: coefficients a_2 in Eq. (1) and respective standard deviations for the selected regions.

ACPD
9, 20853–20880, 2009

Title Page
Abstract Introduction
Conclusions References
Tables Figures
◀I ▶I
◀ ▶
Back Close
Full Screen / Esc
Printer-friendly Version
Interactive Discussion